

# Tailoring Noble Metal-Free Ti@TiO<sub>2</sub> Photocatalyst for Boosting Photothermal Hydrogen Production

1 Sara El Hakim<sup>1</sup>, Tony Chave<sup>1</sup>, Amr A. Nada<sup>2,3</sup>, Stéphanie Roualdes<sup>2</sup>, Sergey I. Nikitenko<sup>1\*</sup>

2 <sup>1</sup>ICSM, Univ Montpellier, UMR 5257, CEA-CNRS-UM-ENSCM, Marcoule, France

3 <sup>2</sup>Institut Européen des Membranes, IEM, UMR 5635, Univ. Montpellier, ENSCM, CNRS,  
4 Montpellier, France

5 <sup>3</sup>Department of Analysis and Evaluation, Egyptian Petroleum Research Institute, Cairo, Nasr City,  
6 P.B. 11727, Egypt

7 \* **Correspondence:**

8 Sergey I. Nikitenko

9 serguei.nikitenko@cea.fr

10 **Keywords: photocatalysis, hydrogen, nanomaterials, titanium suboxide, sonohydrothermal**

## 11 **Abstract**

12 In this work, we provide new insights into the design of Ti@TiO<sub>2</sub> photocatalyst with enhanced  
13 photothermal activity in the process of glycerol reforming. Ti@TiO<sub>2</sub> nanoparticles have been obtained  
14 by sonohydrothermal treatment of titanium metal nanoparticles in pure water. Variation of  
15 sonohydrothermal temperature allows controlling nanocrystalline TiO<sub>2</sub> shell on Ti<sup>0</sup> surface. At  
16 100<T<150°C formation of TiO<sub>2</sub> NPs occurs mostly by crystallization of Ti(IV) amorphous species  
17 and oxidation of titanium suboxide Ti<sub>3</sub>O presented at the surface of Ti<sup>0</sup> nanoparticles. At T>150°C,  
18 TiO<sub>2</sub> is also formed by oxidation of Ti<sup>0</sup> with overheated water. Kinetic study highlights the importance  
19 of TiO<sub>2</sub> nanocrystalline shell for H<sub>2</sub> generation. Electrochemical impedance spectroscopy points out  
20 more efficient electron transfer for Ti@TiO<sub>2</sub> nanoparticles in correlation with photocatalytic data. The  
21 apparent activation energy, E<sub>a</sub>=(25-31)±5 kJ·mol<sup>-1</sup>, assumes that photothermal effect arises from  
22 diffusion of glycerol oxidation intermediates or from water dynamics at the surface of catalyst. Under  
23 the heating, photocatalytic H<sub>2</sub> emission is observed even in pure water.

## 24 **INTRODUCTION**

25 Hydrogen is a clean fuel that, when consumed in a fuel cell, yields only water. Today, 95% of hydrogen  
26 is produced from fossil fuels, such as natural gas and oil (Baykara, 2018). Conversion of solar energy  
27 into hydrogen via photocatalytic splitting of water is an alternative sustainable process of paramount  
28 interest for clean energy storage (Ma et al. 2014; Ghosh, 2018). In this view, preparation of stable and  
29 nontoxic catalysts from non-precious elements showing high photocatalytic activity under solar light  
30 irradiation is of great importance. Among a wide variety of catalysts, titanium oxide, TiO<sub>2</sub>, has been  
31 recognized as one of the most popular photocatalysts. However, TiO<sub>2</sub> can absorb only around 6% of  
32 the sunlight, owing to a quite large bandgap of 3.2 eV for anatase phase (Ghosh, 2018). Another serious  
33 bottleneck of TiO<sub>2</sub> is a rapid electron-hole recombination leading to the decrease in photocatalytic  
34 activity. Therefore, tremendous efforts have been undertaken to narrow bandgap of TiO<sub>2</sub> and to  
35 improve photogenerated charge separation. The recent advances in photocatalysis with TiO<sub>2</sub>-based

36 materials pointed out several strategies of TiO<sub>2</sub> bandgap engineering: doping of TiO<sub>2</sub> with cations or  
37 anions, codoping with cations and anions, self-doping of TiO<sub>2</sub> with Ti<sup>3+</sup>, and surface sensitization with  
38 organic dyes or transition metal complexes (Ma et al. 2014). On the other hand, fabrication of TiO<sub>2</sub>  
39 heterojunctions with other semiconductors, anatase-rutile phase junctions, and TiO<sub>2</sub> loading with  
40 cocatalysts, often noble metal nanoparticles, allows to minimize electron-hole recombination during  
41 the photocatalytic process (Ghosh, 2018).

42 Design of catalyst morphology is another important strategy to reach maximal photocatalytic  
43 activity. Core-shell nanoparticles have attracted a great deal of attention as promising photocatalysts  
44 for hydrogen production due to the synergism between the cores and shells and/or new properties  
45 providing by the interactions between the cores and shells (Gawande et al. 2015). Recently, we reported  
46 strong photothermal effect in the process of photocatalytic hydrogen production from the aqueous  
47 solutions of methanol and glycerol in the presence of noble metal-free Ti@TiO<sub>2</sub> core-shell  
48 nanoparticles (NPs) (Nikitenko et al. 2015, Nikitenko et al. 2018). It is noteworthy that the combination  
49 of photonic and thermal energy could be very beneficial for efficient solar energy harvesting (Ma et al.  
50 2020). However, the mechanism of Ti@TiO<sub>2</sub> formation and the influence of TiO<sub>2</sub> nanocrystalline shell  
51 on the photocatalytic performance have not been examined. In this work, we applied simultaneous  
52 ultrasonic and hydrothermal treatment, called sonohydrothermal treatment (SHT), for the preparation  
53 of Ti@TiO<sub>2</sub> NPs with controlled Ti/TiO<sub>2</sub> ratio. SHT is an emerging environmentally benign technique  
54 effective for the synthesis of nanocrystalline materials with enhanced properties (Nikitenko et al. 2015,  
55 Nikitenko et al. 2018, Cau et al. 2013). Glycerol reforming was used to evaluate the photothermal  
56 performance of prepared Ti@TiO<sub>2</sub> NPs. Glycerol is a low-cost biomass derivative suitable for  
57 hydrogen production (Shimura et al. 2011). Furthermore, quite high boiling point of glycerol (290°C)  
58 allows to study the photothermal effect in a large temperature range. In addition, Ti@TiO<sub>2</sub> NPs have  
59 been studied for the first time using electrochemical impedance spectroscopy (EIS). Combination of  
60 characterization techniques and kinetic study provided new insights into the mechanism of hydrogen  
61 formation and the origin of photothermal effect in studied system.

## 62 MATERIALS AND METHODS

### 63 2.1. Catalyst preparation

64 The commercially available titanium nanopowder (Nanostructured & Amorphous Materials, Inc. Ti,  
65 99%) is an air-sensitive material and it was stored in the argon-filled glove box prior use. Stable  
66 Ti@TiO<sub>2</sub> NPs were prepared by SHT treatment of Ti nanopowder in pure water (Milli-Q 18.2 MΩ·cm  
67 at 25 °C). The SHT reactor is shown in **Supplementary Figure S1** and described previously (Nikitenko  
68 et al. 2015; Nikitenko et al. 2018; Cau et al. 2013). In a typical experiment, 2 g of air passivated Ti  
69 nanopowder was dispersed in 50 mL of water using ultrasonic bath, placed in SHT reactor and heated  
70 at selected temperatures in the range of T = 100–214 °C (autogenic pressure P = 1.0–19.0 bar) under  
71 simultaneous ultrasonic treatment (f = 20 kHz, P<sub>ac</sub> = 17 W) for 3 hours. After cooling, the treated NPs  
72 were recovered by centrifugation, washed with pure water and dried at room temperature under reduced  
73 pressure.

### 74 2.2. Catalyst characterization

75 Powder X-Ray Diffraction (XRD) diagrams were recorded with the use of a Bruker D8 Advance X-  
76 ray diffractometer equipped with a linear Lynx-eye detector (Cu Kα<sub>1,2</sub> radiation, λ = 1.54184 Å). XRD  
77 patterns were collected between 10° and 90° (θ-2θ mode) at room temperature, with a step size of Δ(2θ)  
78 = 0.02° and a counting time of 1.8 s·step<sup>-1</sup>. Quantitative phase analysis was performed by Rietveld

79 refinement with the phase detection limit about 5 % (León-Reina et al. 2016). High-resolution  
80 transmission electron microscopic (HRTEM) and scanning transmission electron microscopic (STEM)  
81 measurements coupled with EDX mapping (SDD Oxford detector) were performed using a Jeol  
82 2200FS (200 kV) microscope. XPS analysis was achieved with an ESCALAB 250 Thermo Electron  
83 device operated under ultra-high vacuum. The excitation source was a monochromatic source (Al-K $\alpha$ ,  
84  $\epsilon = 1486.6$  eV) with a ca. 0.4 mm<sup>2</sup> X-ray spot. The pass energy was fixed at 20 eV. The photoelectron  
85 spectra were calibrated using the Au 4f 7/2 (83.9  $\pm$  0.1 eV) and Cu 2p 3/2 (932.8  $\pm$  0.1 eV)  
86 photoelectron lines. The XPS spectra were treated using AVANTAGE software. The binding energy  
87 scale was established by referencing the adventitious C 1s peak at 284.8 eV. The reflectance spectra  
88 were recorded in BaSO<sub>4</sub> pellets with a Shimadzu UV-3600 spectrophotometer. Thermogravimetric  
89 analysis (TGA) was performed by means of TGA-DTA/DSC Setsys Evolution (Setaram  
90 Instrumentation) device in air flow (900 °C, 10 °C·min<sup>-1</sup>). The concentration of titanium species in  
91 solution after photolysis was measured using SPECTRO ARCOS ICP-OES instrument (detection limit  
92  $\sim$  0.1 ppm).

### 93 **2.3. Electrochemical measurements**

94 Electrochemical Impedance Spectroscopy (EIS) was studied at dark conditions in the frequency range  
95 from 0.1 Hz to 100 kHz with an AC amplitude 10 mV. The electrolytic cell was filled with 1 M KOH  
96 and bubbled with Ar for 20 minutes prior the measurements. Silver / silver chloride (Ag/AgCl) and  
97 platinum (Pt) were used as the reference electrode and counter electrode, respectively. The working  
98 electrode was prepared by ultrasonic dispersion of the synthesized photocatalyst (5 mg) in the mixture  
99 of 1 mL isopropanol (VWR,  $\geq$ 99.7%) and 40  $\mu$ L Nafion (Aldrich, 5 wt% lower aliphatic alcohols, 15-  
100 20% water). Then 5  $\mu$ L of the photocatalyst suspension was deposited onto glassy carbon electrode.

### 101 **2.4. Photothermal hydrogen formation**

102 The photocatalytic study was performed in aqueous glycerol (99 % Sigma-Aldrich) solutions using a  
103 thermostated gas-flow cell made from a borosilicate glass and adapted to mass spectrometric analysis  
104 of the outlet gases. The image of the photocatalytic cell is shown in **Supplementary Figure S2**. In a  
105 typical run, 7.8 mg of photocatalyst was ultrasonically dispersed in 65 mL of aqueous glycerol solution  
106 and placed into the photoreactor. Photolysis was carried out using a white light of ASB-XE-175W  
107 xenon lamp equipped with ozone blocking coatings. The lamp was placed at 8 cm away from the  
108 reactor and the light power at this distance was measured by X1-1 Optometer (Gigahertz-Optik) using  
109 UV-3710-4 (300-420 nm) and RW-3705-4 (400-1100 nm) calibrated detectors. The obtained values of  
110 light power were equal to 8.9 W and 0.6 W for vis/NIR and UV spectral ranges respectively, which  
111 provides the close spectral match to solar spectra. The solutions inside the reactor were stirred  
112 continuously and the temperature was gradually increased up to 95 °C during photolysis. The Ar gas  
113 flow through the reactor was kept constant at 58 mL·min<sup>-1</sup> and controlled by a volumetric flowmeter.  
114 The gaseous products in the outlet gas were analyzed using a Thermo Scientific PRIMA BT mass  
115 spectrometer. The H<sub>2</sub> formation rate was quantified using external calibration curves prepared with  
116 standard gas mixtures in argon (Messer). The water vapors were trapped with molecular sieve (Sigma-  
117 Aldrich, 5 Å) prior to mass spectrometric analysis.

118

119

120

## 121 RESULTS AND DISCUSSION

## 122 3.1. Morphological and structural studies

123 TEM images depicted in **Figure 1A** reveal a quasi-spherical morphology of air passivated Ti particles  
 124 with an average size of around 30-150 nm without any crystals at the surface. On the other hand, EDX  
 125 mapping (**Figure 2A**) indicates the presence of oxygen-enriched layer at the surface of air-passivated  
 126 Ti particles. This layer with a thickness about 11 nm is also clearly distinguishable in the HRTEM  
 127 image of Ti NPs particles in **Figure 1A**. Sonochemical treatment leads to the formation of  
 128 nanocrystalline shell composed of 10-20 nm oxygen-enriched particles, however, formed core-shell  
 129 particles preserve quasi-spherical morphology as it is displayed in **Figures 1B,C and 2B**. We noticed  
 130 that at the SHT temperature of about 100 °C only few nanocrystals are formed, nevertheless their  
 131 amounts increase with the increase of SHT temperature. The average particle size increases on ca. 5-  
 132 10 % after the coating with TiO<sub>2</sub> compared to initial Ti particles.

133 XRD diagram of air passivated Ti NPs in **Figure 3A** displays the patterns of metallic  $\alpha$ -phase  
 134 titanium (JCPDS 00-044-1294) with admixtures of tetragonal nonstoichiometric titanium hydride TiH<sub>x</sub>  
 135 ( $x = 1.53 - 1.97$ , JCPDS 01-079-6209) as it often observed in commercial titanium powders (Ageev et  
 136 al. 1976). However, more thoughtful analysis of XRD data using Rietveld refinement revealed the  
 137 presence of scarce Ti<sub>3</sub>O suboxide with  $P\bar{3}1c$  space group symmetry (Yamaguchi 1969). To the best of  
 138 our knowledge, this is the first observation of Ti<sub>3</sub>O phase at the nanoscale. It is worth noting that the  
 139 XRD diagram of Ti NPs does not exhibit the presence of crystallized Ti(IV) oxides. The XRD data of  
 140 the samples SHT treated at 164 °C and 214 °C clearly point out drop of Ti<sub>3</sub>O content and formation of  
 141 TiO<sub>2</sub> anatase (JCPDS 00-021-1272), which is in line with HRTEM observations (**Figure 1B**).

142 High-resolution Ti 2p XPS spectra shown in **Figure 4** were fitted using binding energies  
 143 published in the NIST database (Wagner et al. 2003). The XPS spectrum of air passivated Ti NPs  
 144 revealed the presence of Ti<sup>0</sup> and lower oxidation states of titanium at the particle surface in agreement  
 145 with the XRD analysis revealed the presence of titanium suboxide in Ti NPs. In contrast to XRD data,  
 146 the XPS spectrum of Ti NPs also exhibits a signal typical for TiO<sub>2</sub> (**Figure 4A**). This discrepancy could  
 147 be assigned to the formation of amorphous hydrated titanium oxide TiO<sub>2</sub>·xH<sub>2</sub>O at the surface of  
 148 metallic titanium. SHT treatment causes disappearance of Ti<sup>0</sup>, TiO, Ti<sub>x</sub>O<sub>y</sub> and Ti<sub>2</sub>O<sub>3</sub> peaks from the  
 149 XPS spectrum and the experimental XPS spectrum of Ti@TiO<sub>2</sub> NPs can be fitted perfectly well by  
 150 defect-free TiO<sub>2</sub> spectrum indicating effective coating of metallic titanium core (**Figure 4B**).

151 **Table 1** summarizes the phase compositions of initial Ti particles and prepared materials  
 152 obtained from the Rietveld refinement of powder XRD data. One can conclude that air passivated Ti  
 153 NPs are stable during the SHT treatment until ca. 100 °C. Further heating until ca. 150 °C causes  
 154 oxidation of Ti<sub>3</sub>O to TiO<sub>2</sub>:



156 At higher temperature, metallic titanium is also oxidized yielding TiO<sub>2</sub>:



158 According to the XPS data anatase nanocrystals at the surface of Ti NPs also can be formed by  
 159 crystallization of TiO<sub>2</sub>·xH<sub>2</sub>O species. It is worth noting that SHT oxidation of Ti NPs is more effective  
 160 than hydrothermal heating without ultrasound (**Table 1**), which was attributed to better heat and mass-  
 161 transfer in the case of SHT process due to the acoustic cavitation, *i.e.* formation, nonlinear oscillations,

162 and implosion of microbubbles formed in the hydrothermal water under the effect of ultrasonic waves  
163 (Cau et al. 2013). Results of TGA analysis displayed in **Supplementary Figure S4** and **Table 2** point  
164 out the increase of titanium metallic core thermal stability with the increase of SHT temperature, which  
165 is explained by the formation of protective TiO<sub>2</sub> shell. It should also be emphasized that the  
166 hydrothermal oxidation of micrometric titanium powder begins at much higher temperature of about  
167 450 °C (Yoshimura et al. 1989), which is most likely related to the particle size effect.

### 168 **3.2. Light absorption and charge transfer**

169 All Ti-based materials studied in this work have intense black color indicating extended photoresponse  
170 with nearly full solar spectrum. The solid state reflectance spectra of both Ti and Ti@TiO<sub>2</sub> NPs (**Figure**  
171 **5**) exhibit a broad band spanning from UV to NIR spectral range, which was attributed to intraband  
172 and interband transitions of metallic Ti (Gawande et al. 2015; Nikitenko et al. 2015). In addition, the  
173 spectra of Ti@TiO<sub>2</sub> NPs reveal an absorption band centered at 220-350 nm typical for the bandgap  
174 transition of crystallized TiO<sub>2</sub>. Kubelka-Munk treatment of the spectral data using  $(F(R)hv)^{1/2}$  vs  $E$   
175 function (López et al. 2012) shown in **Supplementary Figure S5** gives a bandgap energy value of  
176 3.52 and 3.51 eV for SHT 164 °C and SHT 214 °C respectively, which is slightly greater than the  
177 bandgap energy reported for commercial anatase TiO<sub>2</sub> powder ( $E = 3.26$  eV) (López et al. 2012). This  
178 difference may originate from the overlap of Ti<sup>0</sup> interband/intraband transitions and TiO<sub>2</sub> bandgap in  
179 the UV spectral range (**Figure 5**). Kubelka-Munk treatment could lead to the overestimated value of  
180 the bandgap energy in this case.

181 The electrochemical impedance spectroscopy (EIS) provides a valuable information about the  
182 charge transfer and charge recombination processes at the interface of the catalysts and electrolytes  
183 (Barsoukov et al. 2005). **Figure 6** shows the Nyquist plots and the proposed equivalent circuits of the  
184 passivated Ti NPs and Ti@TiO<sub>2</sub> NPs obtained after SHT at 101 °C, 164 °C and 214 °C. The reduced  
185 size of semicircles indicates a lower charge transfer resistance at the particle/electrolyte interface.  
186 Surprisingly, Ti particles coated with TiO<sub>2</sub> nanocrystals exhibit more effective electron transfer than  
187 air-passivated Ti NPs or Ti NPs treated at 101 °C with very low content of TiO<sub>2</sub> NPs at the Ti metal  
188 surface. The resistances calculated for equivalent circuits are summarized in the **Table 3**. The R<sub>1</sub> refers  
189 to the bulk resistance of electrodes and electrolytes, and R<sub>2</sub> represents the resistance at the interface of  
190 the particles and electrolytes. A third resistance R<sub>3</sub> is only observed for Ti@TiO<sub>2</sub> NPs and is most  
191 likely related to the second interface formed between TiO<sub>2</sub> nanoparticles from the shell and Ti<sup>0</sup> core.  
192 Interesting that R<sub>3</sub> increases with the temperature of SHT treatment, or, in other words, with the  
193 increase of TiO<sub>2</sub> anatase content. High R<sub>2</sub> value (9.05 kΩ) for Ti<sup>0</sup> NPs most probably is attributed to  
194 the passivating layer at the metal surface leading to the hindering of charge transfer. Among Ti@TiO<sub>2</sub>  
195 NPs, the sample obtained at 214 °C displays the lowest R<sub>2</sub> value indicating the fastest charge transfer  
196 rate for this material. This conclusion is in an agreement with an effective charge separation in  
197 Ti@TiO<sub>2</sub> NPs recently demonstrated using photoluminescence spectroscopy (Nikitenko et al. 2018).

### 198 **3.3. Photocatalytic hydrogen production**

199 Typical hydrogen emission profiles and calculated H<sub>2</sub> yields for studied photocatalysts shown in  
200 **Figure 7** highlight the crucial role of TiO<sub>2</sub> nanocrystalline shell in the reaction of photocatalytic  
201 glycerol reforming. Kinetic data reveal a clear relationship between the temperature of SHT treatment,  
202 or, in other words, between anatase content in Ti@TiO<sub>2</sub> NPs, and H<sub>2</sub> yield (**Figure 7B**). In addition,  
203 photocatalytic activity correlates with EIS data exhibiting more effective charge transfer for SHT 214  
204 °C NPs. The role of TiO<sub>2</sub> in the reaction mechanism can be understood in terms of the charge separation  
205 between semiconducting TiO<sub>2</sub> shell and metallic Ti<sup>0</sup> core. The optical spectra (**Figure 5**) show that the

206 incident light of the Xe lamp in UV/vis/NIR spectral range is mainly absorbed by Ti<sup>0</sup> core. In  
207 nonplasmonic metal, such as titanium, electron-hole pairs can be created by interband transitions via  
208 nonradiative Landau damping mechanism (Kale et al. 2014). However, in a highly conducting, metallic  
209 material, the electron-hole recombination would be extremely rapid in the absence of hole and/or  
210 electron scavengers. Therefore, one might suggest that in Ti@TiO<sub>2</sub> core-shell NPs TiO<sub>2</sub> provides  
211 effective charge separation, what was confirmed by fluorescence spectroscopy in previous study  
212 (Nikitenko et al. 2018). In addition, TiO<sub>2</sub> can absorb at least part of the UV incident light followed by  
213 electron-hole pairs generation in semiconducting particle. In this case, charge separation would be  
214 provided by electron migration to Ti<sup>0</sup> core, as it occurs in TiO<sub>2</sub> photocatalyst loaded with noble metal  
215 nanoparticles (Ma et al. 2014, Ghosh 2018).

216 Furthermore, photocatalytic process with Ti@TiO<sub>2</sub> NPs exhibits strong photothermal effect in  
217 an agreement with our previous results (Nikitenko et al. 2018). **Figure 7b** demonstrates that the yield  
218 of H<sub>2</sub> increases in ca. 4 times when the bulk temperature increases from 37 °C to 95 °C. On the other  
219 hand, in dark conditions formation of H<sub>2</sub> is not observed even at 95 °C indicating the photonic origin  
220 of studied process. Kinetics of H<sub>2</sub> formation obeys an Arrhenius law (**Supplementary Figure S6**) and  
221 the calculated apparent activation energy, E<sub>act</sub>, for found to be equal to 31±5 and 25±5 kJ·mol<sup>-1</sup> for  
222 SHT 164 °C and SHT 214 °C respectively. It is worth noting that these values are much lower than  
223 the typical activation energy of chemical bonds and has been previously assigned to the diffusion of  
224 intermediates at the catalyst surface (Nikitenko et al. 2018). Alternatively, the temperature dependence  
225 of photocatalytic reactions can be also related to the dynamics of water adsorbed at the surface of the  
226 catalyst (E<sub>act</sub> = 16-21 kJ·mol<sup>-1</sup>, Parrino et al. 2017).

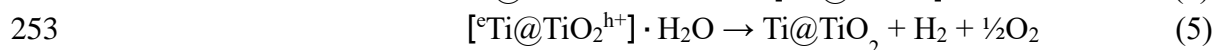
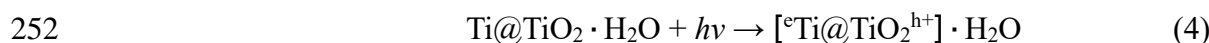
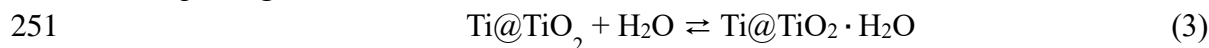
227 **Figure 8** shows the influence of glycerol concentration on H<sub>2</sub> formation with the most active  
228 SHT 214 °C Ti@TiO<sub>2</sub> photocatalyst. The yield of H<sub>2</sub> increases with the glycerol concentration and  
229 then levels off at [Glycerol] ≥ 0.5 M in an agreement with Langmuir-type function indicating that the  
230 mechanism of photocatalytic process involves glycerol adsorption at the active sites of the catalyst.  
231 Similar behavior has been reported for photocatalytic glycerol reforming over Pt/TiO<sub>2</sub> (Jiang et al.  
232 2015) and NiO/TiO<sub>2</sub> (Fujita et al. 2016) NPs. On the other hand, kinetics with Ti@TiO<sub>2</sub> NPs reveals  
233 H<sub>2</sub> emission even from pure water at elevated temperature (**Supplementary Figure S7**). This  
234 observation is largely in agreement with the above conclusion that both water and glycerol can  
235 contribute to the observed photothermal effect.

236 Mass spectrometric measurements indicate the absence of CO<sub>2</sub> emissions (**Supplementary**  
237 **Figure S8**) during the photothermal process with glycerol in consonance with our previous study  
238 (Nikitenko et al. 2018). It is worth noting that photocatalytic glycerol reforming in the presence of  
239 nanocrystalline P25 TiO<sub>2</sub> (83% of anatase and 17 % of rutile) leads to CO<sub>2</sub> and CO formation (Liu et  
240 al. 2014), which implies a certain difference in reaction mechanisms with Ti@TiO<sub>2</sub> and TiO<sub>2</sub>  
241 photocatalysts. We found that in studied system H<sub>2</sub> formation is accompanied by acidification of  
242 photolyte from pH=6 to pH=4 in a ca. 3 h of photolysis indicating formation of some acidic products  
243 without decarboxylation. It has recently been suggested that glycerol is oxidized to glyceric acid in the  
244 studied process (Nikitenko et al. 2018). In addition, it is known that the wet catalytic oxidation of  
245 glycerol can also lead to the formation of other carboxylic acids without decarboxylation, such as  
246 tartronic acid, mesooxalic acid, and hydroxypyruvic acid (Worz et al. 2009).

247 On the basis of the above data, it can be concluded that the mechanism of H<sub>2</sub> formation in  
248 studied system involves two reaction pathways illustrated in **Figure 9**: splitting of water molecules  
249 (equations 3-5 presuming four-electron process) and glycerol reforming (equations 6-12):



250 *H<sub>2</sub>O splitting:*

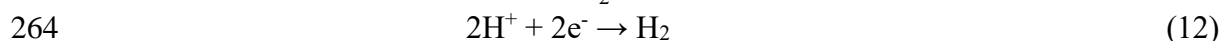
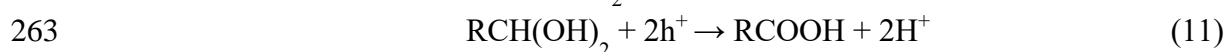
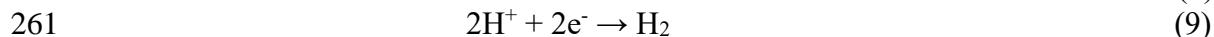
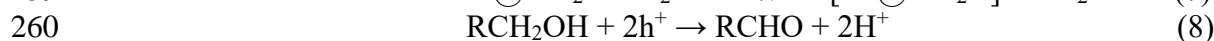
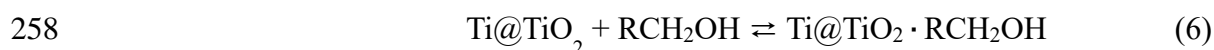


254

255

256 *Glycerol reforming:*

257



265

266 where RCOOH in the equation (11) could represent a mixture of mentioned above carboxylic acids. It  
 267 is worth mentioning that the direct water splitting is practically observable at the sufficiently high  
 268 temperature only. In general, higher yield of hydrogen for glycerol compared to water was attributed  
 269 to more effective hole scavenging by glycerol than by water (Jiang et al. 2015, Tang et al. 2008). The  
 270 link between surface charge carrier dynamics and photocatalytic activity of Ti@TiO<sub>2</sub> NPs is in line  
 271 with this conclusion.

272 Finally, the stability of Ti@TiO<sub>2</sub> photocatalysts at studied conditions was tested using HRTEM  
 273 and ICP-OES techniques. Modification of the particle's morphology was not detected by HRTEM after  
 274 photothermal experiments as shown in **Supplementary Figure S9**. ICP-OES analysis has been  
 275 performed with SPECTRO ARCOS instrument (detection limit of titanium was ca. 0.1 ppm). Particles  
 276 of catalyst have been removed from the reaction mixture by filtration through 0.2 μm PTFE filter prior  
 277 analysis. The ICP-OES analysis after 8 hours of photocatalytic experiments in hot 0.5M glycerol  
 278 solutions revealed a leak of about 0.09 % and 0.29 % of titanium for SHT 214 °C and SHT 164 °C  
 279 Ti@TiO<sub>2</sub> NPs respectively.

280

## 281 CONCLUSIONS

282 In summary, this work provides some new insights into the structure and thermally-assisted  
 283 photocatalytic properties of Ti<sup>0</sup> and Ti@TiO<sub>2</sub> nanoparticles. Rietveld refinement of XRD data revealed  
 284 the presence of scarce titanium suboxide Ti<sub>3</sub>O with a  $P\bar{3}1c$  space group symmetry in raw α-Ti<sup>0</sup> NPs.  
 285 According to STEM/EDX study this species is situated at the surface of Ti<sup>0</sup> NPs. Formation of the  
 286 species with lower oxidation states of titanium was also observed by XPS spectroscopy. Our results  
 287 confirm previous conclusion (Kornilov et al. 1970) about Ti<sub>3</sub>O stability at room temperature.  
 288 Sonohydrothermal synthesis allows to control nanocrystalline TiO<sub>2</sub> shell in Ti@TiO<sub>2</sub> NPs using pure  
 289 water as a solvent. Mechanism of TiO<sub>2</sub> shell formation depends on the SHT temperature: in the  
 290 temperature range 100-150 °C TiO<sub>2</sub> is formed mainly by the oxidation of Ti<sub>3</sub>O, and oxidation of Ti<sup>0</sup> to  
 291 TiO<sub>2</sub> occurs at higher temperature. Coating of titanium metal nanoparticles with anatase nanocrystals

292 provides their better stability to oxidation and strong photothermal effect of hydrogen production from  
293 aqueous glycerol solutions. In a hot water, photocatalytic formation of hydrogen is observed even  
294 without glycerol. However, the yield of hydrogen in the presence of glycerol is higher than that in pure  
295 water, which can be related to more effective scavenging of photogenerated holes with glycerol.  
296 Glycerol reforming leading to hydrogen production is not accompanied by CO<sub>2</sub> emission in studied  
297 system. The acidification of the photolyte solution implies that glycerol is oxidized to some acidic  
298 products, most probably, to the mixture of organic acids derived from glycerol. The apparent activation  
299 energy  $E_{\text{act}} = (25-31) \pm 5 \text{ kJ} \cdot \text{mol}^{-1}$  of studied process is much lower than the typical activation energy  
300 of chemical bonds indicating that the origin of the photothermal effect is related to the diffusion of  
301 intermediates arise from glycerol or from the dynamics of water adsorbed at the surface of the catalyst.

## 302 DATA AVAILABILITY STATEMENT

303 The original contributions presented in the study are included in the article/supplementary materials,  
304 further inquiries can be directed to the corresponding author/s.

## 305 AUTHOR CONTRIBUTIONS

306 All authors contributed to this work. S. I. N. and S. R. conceived the study, S. I. N., S. R., T. C., and  
307 S. E. H. prepared the manuscript, T. C. and S. E. H. prepared the samples and performed their  
308 characterization, S. E. H. and S. I. N. performed photocatalytic experiments, A. A. N. and S. E. H.  
309 performed electrochemical study. All authors approved the submitted version.

## 310 FUNDING

311 This work has been partially funded by the CNRS Energy unit (Cellule Energie) through the project  
312 "PHOTOCAT.Ti@TiO2.H2".

## 313 ACKNOWLEDGMENTS

314 The authors kindly acknowledge Dr. Adel Mesbach for Rietveld refinement of XRD data, Dr. Xavier  
315 Le Goff for HRTEM measurements, Dr. Cyrielle Rey for TGA measurements and Dr. Valerie Flaud  
316 for XPS analysis.

317

## 318 REFERENCES

- 319 Ageev, N. V., Babareko, A. A., Rubina, E. B., Betsofen, S. Ya., and Bunin, L. A. (1976) X-ray  
320 diffraction analysis of titanium hydrides in commercial titanium alloys. *Met. Sci. Heat Treat.* 18, 124-  
321 130. UDC 621.386.8:669.295
- 322 Barsoukov, E. and Macdonald, J. R. (Eds.). (2005) Impedance spectroscopy: theory, experiment, and  
323 applications, Wiley-Interscience, New Jersey, USA.
- 324 Baykara, S. Z. (2018) Hydrogen: A brief overview on its sources, production and environmental  
325 impact. *Int. J. Hydrogen Energy*, 43, 10605-10614. doi: 10.1016/j.ijhydene.2018.02.022



- 326 Cau, C., Guari, Y., Chave, T., Larionova, J., Pochon, P., and Nikitenko, S. I. (2013) Sonohydrothermal  
327 synthesis of nanostructured (Ce,Zr)O<sub>2</sub> mixed oxides with enhanced catalytic performance. *J. Phys.*  
328 *Chem. C*, 117, 22827-22833. doi: 10.1021/jp407096p
- 329 Fujita, S.-I., Kawamori, H., Honda, D., and Arai, M. (2016) Photocatalytic hydrogen production from  
330 aqueous glycerol solution using NiO/TiO<sub>2</sub> catalysts: effects of preparation and reaction conditions.  
331 *Appl. Cat. B: Environ.* 181, 818-824. doi: 10.1016/j.apcatb.2015.08.048
- 332
- 333 Gawande, M. B., Goswami, A., Asefa, T., Guo, H., Biradar, A. V., Peng, D.-L., Zboril, R., and Varma,  
334 R. S. (2015) Core-shell nanoparticles: synthesis and applications in catalysis and electrocatalysis.  
335 *Chem. Soc. Rev.*, 44, 7540-7590. doi: 10.1039/C5CS00343A
- 336 Ghosh, S. (2018) Visible-light-active photocatalysis: nanostructured catalyst design, mechanisms and  
337 applications, Wiley-VCH, Mörlenbach, Germany.
- 338 Jiang, X., Fu, X., Zhang, L., Meng, S., and Chen, S. (2015) Photocatalytic reforming of glycerol for  
339 H<sub>2</sub> evolution on Pt/TiO<sub>2</sub>: fundamental understanding the effect of co-catalyst Pt and the Pt deposition  
340 route. *J. Mater. Chem.* 3, 2271-2282. doi:10.1039/C4TA06052K
- 341 Kale, M. J., Avanesian, T., and Christopher, P. (2014) Direct photocatalysis by plasmonic  
342 nanostructures. *ACS Catal.* 4, 116-128. doi: 10.1021/cs400993w
- 343 Kornilov, I. I., Vavilova, V. V., Fykin, L. E., Ozerov, R. P., S.P. Soloviev, S. P. and Smirnov, V. P.  
344 (1970) Neutron diffraction investigation of ordered structures in the titanium oxygen system. *Metal.*  
345 *Mater. Trans. B*, 1, 2569-2571. doi: 10.1007/BF03038386.
- 346 León-Reina, L., García-Maté, Álvarez-Pinazo, M. G., Santacruz, I., Vallcorba, O., De la Torre, A. G.,  
347 and Aranda M. A. G. (2016) Accuracy in Rietveld quantitative phase analysis: a comparative study of  
348 strictly monochromatic Mo and Cu radiations. *J. Appl. Cryst.*, 49, 722-735. doi:  
349 10.1107/S1600576716003873
- 350 Liu, R., Yoshida, H., Fujita, S.-I., and M. Arai, M. (2014) Photocatalytic hydrogen production from  
351 glycerol and water with NiO<sub>x</sub>/TiO<sub>2</sub> catalysts. *Appl. Cat. B: Environ.* 144, 41-45. doi:  
352 10.1016/j.apcatb.2013.06.024
- 353 López, R., and Gómez, R. (2012) Band-gap energy estimation from diffuse reflectance measurements  
354 on sol-gel and commercial TiO<sub>2</sub>: a comparative study. *J. Sol-Gel Sci. Technol.* 61, 1-7. doi :  
355 10.1007/s10971-011-2582-9
- 356 Ma, R., Sun, J., Li, D. H., and Mei, J. J. (2020) Review of synergetic photo-thermo-catalysis:  
357 mechanisms, materials and applications. *Int. J. Hydrogen Energy*, 45, 30288-30324. doi:  
358 10.1016/j.ijhydene.2020.08.127
- 359 Ma, Y., Wang, X., Jia, Y., Chen, X., Han, H., and Li, C. (2014) Titanium dioxide-based nanomaterials  
360 for photocatalytic fuel generations. *Chem. Rev.* 114, 9987-10043. doi: 10.1021/cr500008u

- 361 Nikitenko, S. I., Chave, T., Cau, C., Brau, H.-P., and Flaud, V. (2015) Photothermal hydrogen  
362 production using noble-metal-free Ti@TiO<sub>2</sub> core-shell nanoparticles under visible-NIR light  
363 irradiation. *ACS Catal.* 5, 4790-4795. doi: 10.1021/acscatal.5b01401
- 364 Nikitenko, S. I., Chave, T., and Le Goff, X. (2018) Insights into the photothermal hydrogen production  
365 from glycerol aqueous solutions over noble metal-free Ti@TiO<sub>2</sub> core-shell nanoparticles. *Part. Part.*  
366 *Syst. Charact.* 35, 1800265. doi: 10.1002/ppsc.201800265
- 367 Parrino, F., Conte, P., De Pasquale, C., Laudicina, V. A., Loddo, V., and Palmisano, L. (2017) Nature  
368 of interactions at the interface of two water-saturated commercial TiO<sub>2</sub> polymorphs. *J. Phys. Chem. C*,  
369 121, 2258-2267. doi: 10.1021/jp400298m
- 370 Shimura, K., and Yosida, H. (2011) Heterogeneous photocatalytic hydrogen production from water  
371 and biomass derivatives. *Energy Environ. Sci.* 4, 2467-2481. doi: 10.1039/C1EE01120K
- 372 Tang, J., Durrant, J. R., and Klug, D. R. (2008) Mechanism of photocatalytic water splitting in TiO<sub>2</sub>.  
373 Reaction of water with photoholes, importance of charge carrier dynamics, and evidence for four-hole  
374 chemistry. *J. Am. Chem. Soc.* 130, 13885-13891. doi: 10.1021/ja8034637
- 375 Wagner, C. D., Naumkin, A., Kraut-Vass, A., Allison, J. W., Powell, C. J., and Rumble, J. R. (2003)  
376 NIST standard reference database 20, version 3.4. <http://srdata.nist.gov/xps/>
- 377 Worz, N., Brandner, A., and Claus, P. (2009) Platinum–bismuth-catalyzed oxidation of glycerol:  
378 kinetics and the origin of selective deactivation. *J. Phys. Chem. C*, 114, 1164-1172. doi:  
379 10.1021/jp909412h
- 380 Yamaguchi, S. (1969) Interstitial order-disorder transformation in the Ti-O solid solution. I. Ordered  
381 arrangement of oxygen. *J. Phys. Soc. Jpn.* 27, 155-163. doi: 10.1143/JPSJ.27.155
- 382 Yoshimura, M., Ohira, H., Sōmiya, S. (1989) Formation of TiO<sub>2</sub> and ZnO powders by hydrothermal  
383 oxidation of Ti and Zn metals. In: Sōmiya S. (Ed.) Hydrothermal reactions for materials science and  
384 engineering. Springer, Dordrecht. doi: 10.1007/978-94-009-0743-0\_17

385

386

387

388

389

390

391

392

393

## 394 TABLES

395 **Table 1.** Variation of Ti NPs composition with the temperature of SHT treatment obtained by Rietveld  
 396 refinement of XRD patterns. Time of treatment was equal to 3 h.

Sample	mol.% ( $\pm 5\%$ )		
	Ti	Ti <sub>3</sub> O	TiO <sub>2</sub> anatase
Air passivated Ti*	86	14	--
SHT 101 °C	88	12	--
HT 150 °C **	88	5	7
SHT 164 °C	$\geq 80.5$	$\leq 1.5$	18
SHT 214 °C	$\geq 62$	$\leq 3$	35

397 \*The admixture of TiH<sub>x</sub> and amorphous TiO<sub>2</sub>·xH<sub>2</sub>O species were not  
 398 taken into account. \*\*HT stands for hydrothermal treatment without  
 399 ultrasound. XRD and TEM data for these NPs are shown in  
 400 **Supplementary Figure S3.**

401

402 **Table 2.** Thermal stability of Ti and Ti@TiO<sub>2</sub> NPs obtained from TGA analysis. T<sub>ox</sub> indicates the  
 403 beginning of metallic titanium core oxidation calculated as it shown in Supplementary Figure S4.

Sample	Air passivated Ti	SHT/101 °C	SHT/164 °C	SHT 214 °C
T <sub>ox</sub> $\pm 10$ °C	230	240	263	304

404

405 **Table 3.** EIS parameters for Ti and Ti@TiO<sub>2</sub> NPs.

Samples	R <sub>1</sub> ( $\Omega$ )	R <sub>2</sub> ( $\Omega$ )	R <sub>3</sub> (k $\Omega$ )
Ti@TiO <sub>2</sub> SHT 214 °C	59.95	7.96	5.44
Ti@TiO <sub>2</sub> SHT 164 °C	48.63	22.85	7.67
Ti@TiO <sub>2</sub> SHT 101 °C	42.06	34.03	9.12
Air passivated Ti NPs	49.84	9.05 (k $\Omega$ )	not been observed

406

407

408

409

410 **FIGURE CAPTIONS**

411 **Figure 1.** Typical TEM images of initial Ti particles (A), SHT-treated particles in water at 101 °C (B)  
412 and >150 °C (C). The distance of 0.35 nm corresponds to (101) plane of TiO<sub>2</sub> anatase.

413 **Figure 2.** STEM/EDX mapping of air passivated Ti<sup>0</sup> NPs (A) and SHT-treated at 164 °C Ti@TiO<sub>2</sub>  
414 NPs (B), green dots – Ti, red dots - O.

415 **Figure 3.** XRD patterns of the initial Ti NPs and Ti@TiO<sub>2</sub> NPs treated at different temperatures under  
416 SHT conditions (A). Zoom of the figure (A) in 39-41 2θ° range indicating the decrease in Ti<sub>3</sub>O content  
417 with increasing of SHT temperature (B). Example of Rietveld fit of the XRD diagram for Ti NPs in  
418 39-41 2θ° range indicating the presence of Ti<sub>3</sub>O phase (C), red line – Ti<sub>3</sub>O, black line – α-Ti.

419 **Figure 4.** Fitted Ti 2p high-resolution XPS spectra of air-passivated Ti<sup>0</sup> (A) and SHT/214 °C Ti@TiO<sub>2</sub>  
420 (B) NPs. Red line indicates experimental spectrum.

421 **Figure 5.** Solid-state reflectance spectra of Ti<sup>0</sup> NPs before and after sonohydrothermal treatment at  
422 different temperatures. The spectrum of Ti particles SHT treated at 101 °C is very similar to the  
423 spectrum of air-passivated Ti<sup>0</sup> particles reported recently (Nikitenko et al. 2015).

424 **Figure 6.** Nyquist plots for Ti<sup>0</sup> NPs and Ti@TiO<sub>2</sub> NPs and the equivalent circuit for Ti<sup>0</sup> (A) and  
425 Ti@TiO<sub>2</sub> (B).

426

427 **Figure 7.** Typical hydrogen emission profiles with catalysts obtained at 101 °C, 164 °C and 214 °C  
428 SHT temperatures in solutions of 0.5 M glycerol under Xe-lamp white light and Ar flow (A), and H<sub>2</sub>  
429 yields in 0.5 M glycerol solutions and pure water for SHT-214°C catalyst (B). The uncertainty for H<sub>2</sub>  
430 yields was estimated about 10-15 %.

431

432 **Figure 8.** Plot of the H<sub>2</sub> formation yields against glycerol concentrations over SHT 214 °C Ti@TiO<sub>2</sub>  
433 photocatalyst at 53 °C and 87 °C.

434

435 **Figure 9.** Graphical sketch of suggested mechanism of H<sub>2</sub> photocatalytic formation in the presence of  
436 Ti@TiO<sub>2</sub> core-shell nanoparticles.

437 **Conflict of Interest:** The authors declare that the research was conducted in the absence of any  
438 commercial or financial relationships that